

**Dynamic pressure evolution during the LHC operation**S. Bilgen<sup>1</sup>, G. Sattonnay<sup>1,\*</sup>, B. Mercier<sup>1</sup>, V. Baglin<sup>2</sup>, and B. Henrist<sup>2</sup><sup>1</sup>*IJCLab, University Paris Saclay, CNRS/IN2P3, 15 Rue Georges Clemenceau, 91400 Orsay, France*<sup>2</sup>*European Organization for Nuclear Research, CERN, 1211, Geneva 23, Switzerland*

(Received 15 February 2022; accepted 22 July 2022; published 29 August 2022)

For the accelerator community and the vacuum scientists, the understanding of the beam interactions with a vacuum chamber is fundamental to provide solutions to mitigate pressure rises induced by electron, photon, and ion molecular desorption. Moreover, beam instabilities induced by ion and electron clouds must be investigated in order to find solutions to reduce them. This study presents *in situ* measurements of pressure evolutions and electrical currents performed during the LHC RUN II (2018). The proton beam circulating in the LHC vacuum chamber ionizes the residual gas producing electrons as well as positive ions. These charged particles are accelerated away from the beam and reach the vacuum chamber wall, inducing, among other phenomena, stimulated desorption and secondary electron emission. Moreover, protons emit synchrotron radiations that also induce photodesorption and photoelectron production. Experimental measurements of the electrical signals recorded on copper electrodes were compared to calculations considering both the secondary electron yield of copper and the electron energy distribution. All measurements performed with the Vacuum Pilot Sector in the LHC ring show the importance of taking into account a large variety of phenomena in order to understand the pressure evolution in the LHC. Results show that the multipacting threshold, corresponding to an increase in the electron cloud density, strongly depends on the number of protons per bunch. Finally, the ion current was measured with a biased electrode lower than  $-500$  V. It was much higher than expected, pointing its origin not only from simple beam-gas ionization but also from the ionization of the residual gas by the electron cloud.

DOI: [10.1103/PhysRevAccelBeams.25.083101](https://doi.org/10.1103/PhysRevAccelBeams.25.083101)**I. INTRODUCTION**

High energy particle colliders (above several GeV) are used to explore the structure of matter, such as the Large Hadron Collider (LHC) operated by the CERN, SuperKEKB in Japan, and RHIC at Brookhaven National Laboratory in New York. One of the main parameters to characterize the performance of a particle accelerator by physicists is the luminosity of the beam which provides a measure of how many collisions per unit time are happening in the accelerator. Achieving high luminosity is one of the major challenges faced by colliders to detect rare events. The luminosity optimization of the LHC, its upgrade (HL-LHC), and the goal value for future high-energy hadron colliders (FCC) highlight one of the potential main limitations of these machines: the dynamic pressure. Energetic charged particles interact with gas molecules and these interactions cause many unwanted effects, such as a loss of the accelerated particles (leading to material activation or background to the

detectors), the change of the charge state, residual gas ionization, and the creation of a charged particle cloud (electrons for positive accelerated particle beams or ions for accelerated electron beams). The space charge affects the beam quality, leading to beam emittance growth and beam instabilities. It is worth noting that all of these dynamic pressure phenomena represent one of the most important limitations to reach the ultimate luminosity. Such drawbacks limit the accelerator performances and represent a real barrier for high-energy physics research.

The LHC is currently the world's largest particle accelerator. It is designed to accelerate and collide two counter-rotating particle beams, called beam 1 (or blue beam) and beam 2 (or red beam), of either protons up to an energy of 7 TeV or lead nuclei up to 574 TeV per nucleus [1,2]. Along its path, the beam ionizes the residual gas inside the LHC beam pipe ring causing the production of electrons and positive ions, which then move under the action of the beam field forces and their own space charge. The presence of electrons, from which a multipacting process may get started, eventually leads to the buildup of a quasistationary electron cloud (EC) [3–6].

This EC buildup is initiated with the generation of free electrons resulting from the residual gas ionization caused by the beam passage and the photoelectron production due to Synchrotron Radiation (SR) coming from bending

\*[gael.sattonnay@ijclab.in2p3.fr](mailto:gael.sattonnay@ijclab.in2p3.fr)

Published by the American Physical Society under the terms of the [Creative Commons Attribution 4.0 International license](https://creativecommons.org/licenses/by/4.0/). Further distribution of this work must maintain attribution to the author(s) and the published article's title, journal citation, and DOI.

magnets. These primary electrons are then attracted toward the center of the beam pipe by the bunched beam electric field, increasing their energy up to a maximum of few thousand eV [5]. Once the proton bunch passes, the electrons can continue their path and impinge the beam pipe walls, producing secondary electrons (SEs). These latter have usually low energy, i.e., only a few eV above the material work function ( $WF \approx 4.5$  eV for Cu) [7]. In turn, these secondary electrons are accelerated by the following proton bunches and can produce new electrons, amplifying bunch by bunch the number of electrons. It is worth noting that photoelectron production can have a strong impact on the EC dynamics, more particularly for beams with an energy higher than 2.5 TeV in the LHC. At this beam energy, the critical energy of the SR power spectrum is around 2 eV and a significant fraction of the photons has enough energy to stimulate the photoelectron emission [8]. EC effects have been recognized among the major performance limitations for the LHC. They were observed at the LHC during the first 3 years of beam operation (Run I, 2010–2012) and become more and more severe while moving to tighter bunch spacing necessary to reach the design luminosity within the pileup limits required by the LHC experiments. Detrimental effects are associated with this phenomenon, such as pressure rises or heat loads deposited on beam pipe walls and on the cold bore of the superconducting magnets (with the major risk of a “quench” of the magnets), and emittance growth. So, to investigate pressure changes, electron, and/or ion creations related to the LHC operation, we performed measurements in a sector of the LHC ring dedicated to the monitoring of these phenomena: the Vacuum Pilot Sector (VPS) during the LHC RUN II (May, July, and October 2018) using a bunched proton beam.

## II. EXPERIMENTAL MEASUREMENT IN THE VACUUM PILOT SECTOR

### A. The vacuum pilot sector—VPS

The Vacuum Pilot Sector is installed in the LHC ring on the left side of the interaction point 8 (LHCb experiment) in a room temperature area, originally made of standard drift 80 mm ID vacuum chambers, in vacuum sector A5L8 between the quadrupoles Q4 and Q5. It allows for monitoring the pressure and electron cloud during machine operation [8–11]. In addition, the VPS allows investigations of new surfaces, coatings, and chemical treatments of materials aiming at improving the LHC beam performance and studying LHC upgrades. This facility is composed of a double vacuum sector (two separated beams) with a length of about 18 m. Dedicated detectors are installed along the sectors at four different places (stations). The symmetry is kept everywhere to be able to compare the results on both lines. Each station is composed of two parallel opposite vessels with similar equipments. However, each station

could have different surface materials under test and possibly different apparatus. A strong pumping must be set up between each station to limit gas transfer from one to the other. This is achieved by the use of 2-m long NEG-coated beam pipes and ion pumps on both sides of each station. We focused our investigation on the station 4 (beam 1) made of unbaked copper representing the surface in the LHC installed in 2016.

Eight square windows are available in each liner to install different types of detectors. Electron flux measurements can be performed with different kinds of grids and electrodes [9–11]: (i) A detector equipped with a single grid, with 7% of transparency, to acquire electrical signals of the electron cloud. Usually, a positive voltage bias of 9 V is applied to the collector in order to recapture secondary electrons emitted when the incident electrons impinge the electrode surface. A specific collector exists also with a variable bias from +1000 V to –1000 V. (ii) A detector with a double grid: the first grid with 7% of transparency; a second grid (75% of transparency) polarizable down to –1000 V to perform an energy filter of electrons and the electron collector polarized at +9 V. This detector is used to record the energy spectrum of the electron cloud.

Each station has a single grid detector in the up position to record the electron activity with time. A low current multiplexer, using 20 lines, measures the pickup signals during operation (Keithley Model numbers 7001, 7158, and 6485). Pressure, gas composition, and beam parameters can also be monitored and the signals are recorded during a proton run to follow the behavior of the different surfaces.

### B. Electrical measurement strategy

When a material is exposed to electron irradiation, it emits secondary electrons. Therefore, the measuring electrode must be positively biased to ensure any SEs emitted from the electrode are returned to the electrode to record a correct electron intensity. If this method is not applied, the recorded current  $I_{\text{electrode}}$  will be  $I_{\text{electrode}} = I_{e^-} - I_{\text{SE}}$  where  $I_{e^-}$  is the primary electron current and  $I_{\text{SE}}$  is the emitted SE current. In this latter case, the incident electron current will be underestimated because  $I_{\text{SE}}$  is negative (Fig. 1).

Conversely, to detect positive ions, following, e.g., the ionization of residual gas in the vacuum chamber, a negative bias must be applied to the electrode. However, in this bias scheme, an electrode subjected to both electron and ion fluxes will record a positive current due to either positive ions or SEs, or both of them. Nevertheless, an electrode bias with a sufficiently high negative value should allow the repelling of all incident electrons and minimize the SE production and finally should lead to the collection of only positive ions. This strategy strongly depends on the electron energy distribution in the beam pipe.

This investigation was focused more specifically on the impact during the LHC operation of ions produced in the station 4 of the VPS (beam 1 and 80 °C baked copper liner).

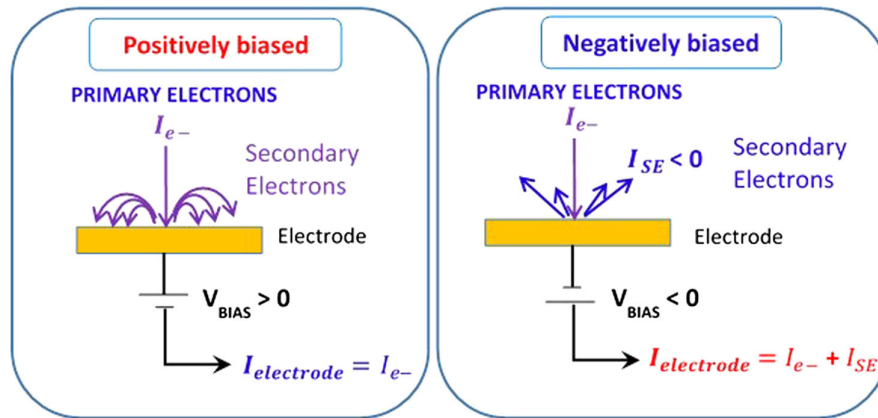


FIG. 1. Basic schematic of the electron current measurement with a positive (left) and a negative bias (right) electrode.

A negatively biased copper electrode was used to collect positive charges (electrode K6517A with 7% transparency). This electrode could be polarized from a voltage  $V_{\text{bias}} = +127$  to  $-127$  V first, and after modifications during a technical stop, from  $+1000$  V to  $-1000$  V. The possibility to apply a negative bias voltage gave us the opportunity to detect positive ions. In the same station, the pressure (measured with a Bayard Alpert gauge) and the electron current were also monitored by two positively biased electrodes polarized at  $+9$  V: the K11 y electrode with a 0.2% transparency grid (simple grid) and the K12 electrode, called also the electron kicker detector (EKD, double grid) initially used as an energy filter to obtain the electron spectrum.

The variation of collected currents with both energy and beam intensity during a fill will be discussed in detail in the next section. As seen in Fig. 1, the electrical signals recorded by the different electrodes and the pressure signal have similar evolutions during a standard fill. It is worth noting that, in the plot of the electron current (that is a negative value), the y axis was reversed to show the variation of the electron intensity in the same way as the positive data. This convention will be applied to all plots in this work.

Despite all electrodes being biased to  $+9$  V (the inner grid of the EKD being set to 0 V), the maximum value of the electron current is different between electrodes due to the fact that (i) the grid transparency is not the same (7% for K6517A, 5.3% for EKD, and 0.2% for K11); (ii) they are installed in the same station 4 but at different positions relative to the beam.

It should be emphasized that when the K6517A electrode is polarized negatively to detect ions, the electron measurement at the same spot is lost. However, the ratio between the electron current measured by the K6517A and the K11 electrodes (with a bias voltage of  $+9$  V for both) on one side, and the ratio between the intensity measured by the K6517A and EKD electrodes (upper grid not polarized and collector at  $+9$  V) on the other side, remains constant on all fills measured. Thus, when K6517A is negatively polarized

to measure ions, the electron current, which should have been measured by this electrode, can be extrapolated from the current measurements carried out at the same time with K11 Eq. (1) and EKD Eq. (2) using the following expressions:

$$IK6517A(+9 \text{ V}) = 24.31K11(+9 \text{ V}) \quad (1)$$

$$IK6517A(+9 \text{ V}) = 1.42I_{\text{EKD}}(+9 \text{ V}), \quad (2)$$

where factors 24.3 and 1.42 were experimentally determined by measuring simultaneously the current with K11 and K6517A biased both at  $+9$  V. It was checked that these factors remain constant for several fills recorded at different periods.

Since this specific electrode was also used to carry out other studies, measurements of ions were performed with the negatively biased electrode only during May, July, and October 2018.

### III. MEASUREMENTS IN THE VPS

#### A. Pressure and electrical currents during a standard fill for physics

Figure 2 shows measurements performed during the fill 7319 (a standard fill with a beam structure: 25ns\_2556b\_144bpi\_20inj corresponding to a beam with 25 ns bunch spacing, composed of 2556 bunches, with 144 bunches per injection step injected in LHC in 20 injections). For this fill, the K6517A electrode was polarized at  $-600$  V. The pressure, the electron current, and the positive current follow the same behavior along the time. Two major bumps of recorded signals are observed: the first one during the beam injection and the second one during the energy ramp-up. Four steps may be distinguished [6]: (i) Injection of protons into the ring. More protons circulate, more ionizations of the residual gas are produced and an increase in both the pressure and the electrical current is observed. After the injection, a slight decrease of the beam intensity is observed due to

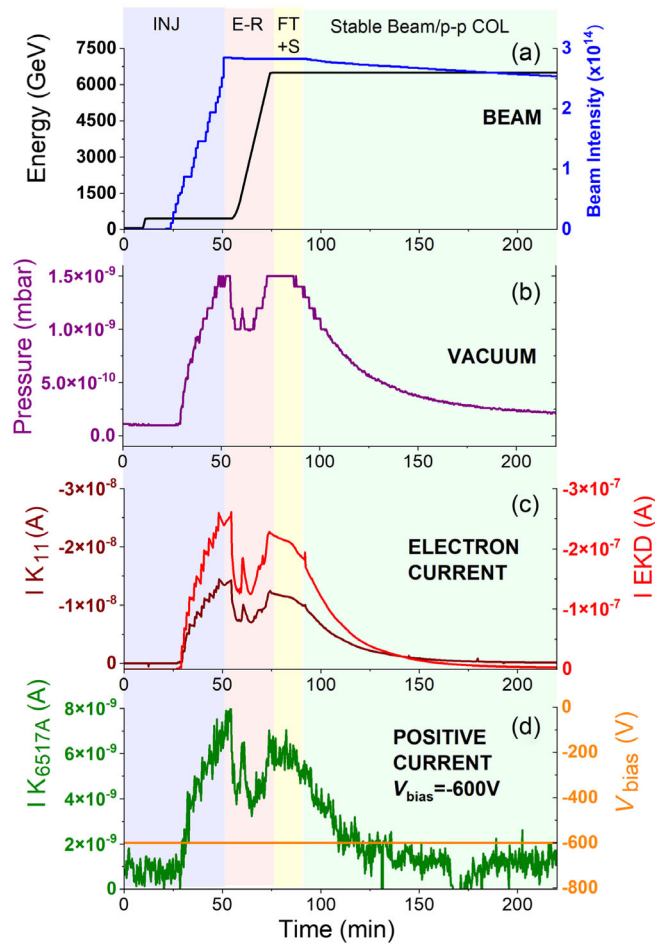


FIG. 2. Measurements performed in station 4 of the VPS during fill 7319: Energy and intensity of the beam 1 (a), pressure measured with a Bayard Alpert gauge (b), electron current collected with the K11 and EKD electrodes (biased at +9 V, the inner grid of EKD being not polarized in this case) (c), positive current collected with the K6517A electrode polarized at  $-600$  V (d); (INJ = injection, E-R = Energy, Ramp, FT + S = Flat, Top, and Squeeze).

proton losses along their path; (ii) Energy ramp-up. The evolution of the measurements during this step depends on two main effects. First, the pressure and the electrical signal variations are related to the modifications of the energy spread (depending on both the bunch length and the rf) due to the rf noise injected to mitigate the longitudinal beam instability. Second, at 2.8 TeV, the main contribution comes from the photoelectrons that are interacting with the residual gas and the chamber walls; (iii) Stable beam; (iv) Beginning of proton-proton collisions. In these two latter steps, the proton intensity decreases due to proton losses, leading to the decrease in both the electrical signals and the pressure.

### B. Increase of pressure during beam injection (at 450 GeV without synchrotron radiation)

When the evolution of the pressure during the injection ( $E_{\text{beam}} = 450$  GeV) for the standard filling pattern of a fill

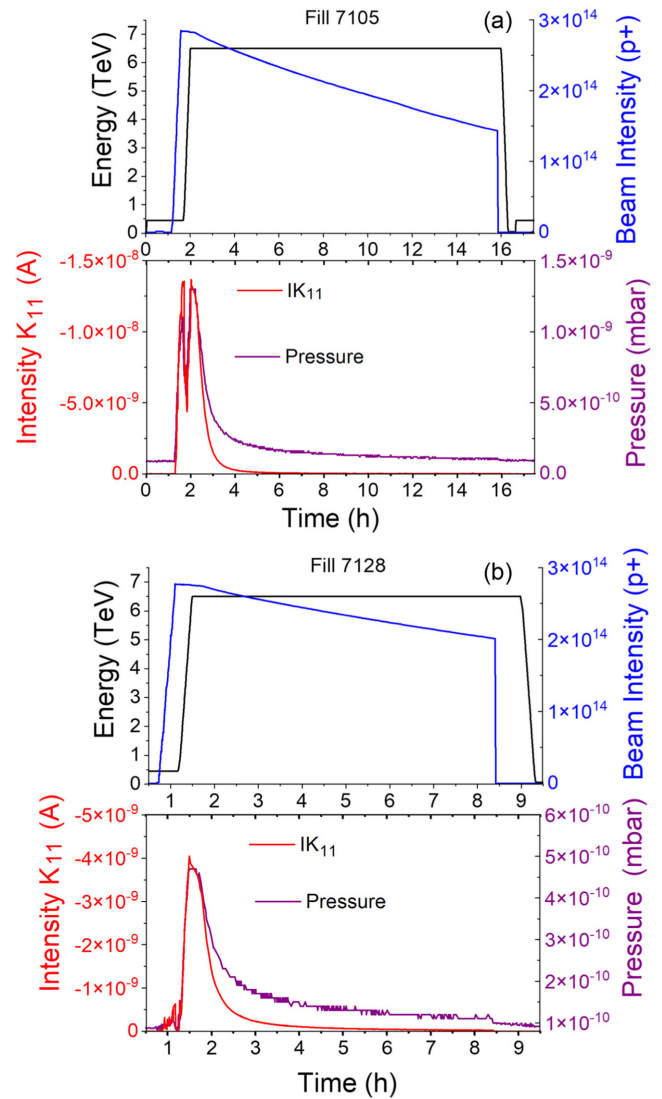


FIG. 3. Energy and intensity of beam 1 (top), electron current and pressure (bottom) during fills 7105 (a) and 7128 (b), respectively.

for physics is carefully analyzed, differences are observed depending on fills. Figure 3 shows a comparison of pressure changes for fills 7105, 7127, and 7128. They were recorded during the same period with the same filling pattern so that the differences are not due to conditioning effects or different beam patterns. An increase in pressure is actually observed during the injection of the proton bunches during fill 7105 (the maximum pressure reaches a value of  $9.5 \times 10^{-10}$  mbar), but it remains very low for fill 7127 ( $3 \times 10^{-10}$  mbar) or even almost nonexistent for fill 7128. On the contrary, an increase in the pressure during the energy ramp was always observed for all fills.

In order to explain the above-described phenomenon, the influence of several parameters was studied, in particular, (i) the initial pressure before injection; (ii) the proton beam intensity; (iii) the number of protons per bunch (nppb). The influence of the nppb has been repeatedly identified as an

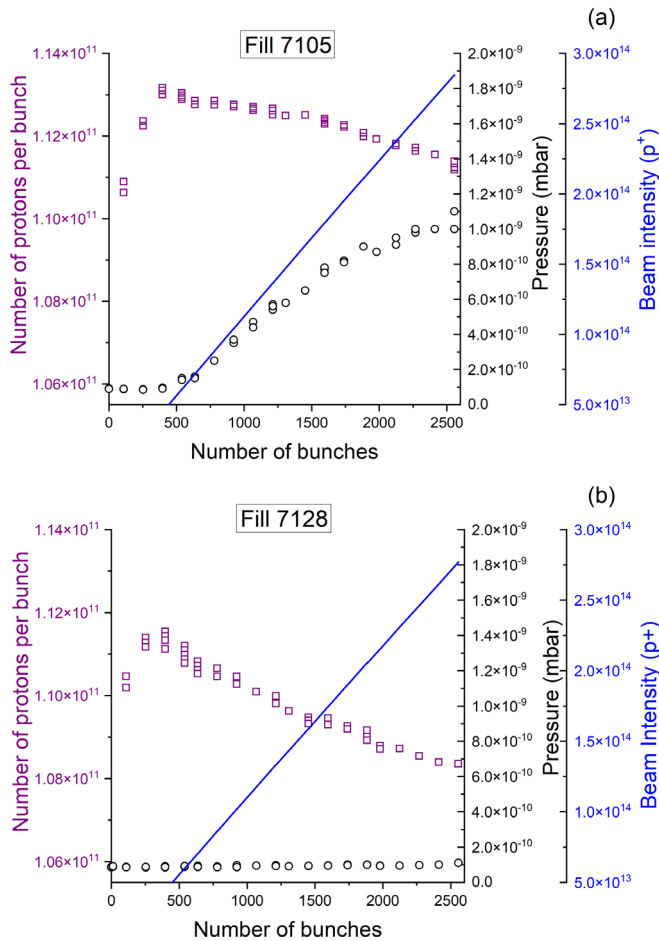


FIG. 4. Evolution of the number of protons per bunch, pressure and intensity of beam 1 in station 4 as a function of the number of bunches during injection at 450 GeV for fill 7105 (a) and fill 7128 (b), respectively.

important parameter that controls the creation of electron clouds (e.g., in [4]). Figure 4 compares the nppb during injection and the pressure variation in station 4 (the intensity of the beam 1 is given for information) as a function of the number of bunches injected in the ring, for standard fills 7105 and 7128. The nppb is here calculated from the intensity of the beam at a given time divided by the number of bunches circulating in the ring at the same time. Thus, it represents an average value of the nppb. In fill 7105, when the nppb exceeds a threshold of  $1.12 \times 10^{11}$  p + /bunch (number of protons per bunch), the pressure rises, whereas it remains low and does not evolve below this limit (while the beam intensity is almost the same) for fill 7128.

Therefore, the nppb appears to be a key parameter that controls the EC formation, and, consequently, the pressure rises during the beam injection step due to electron stimulated desorption. However, is the threshold value the same for all fills? Figures 5 and 6 show the evolution of the nppb for a set of standard fills recorded at two different periods. It can be clearly seen that fills for which a rise of pressure is observed are those for which the nppb

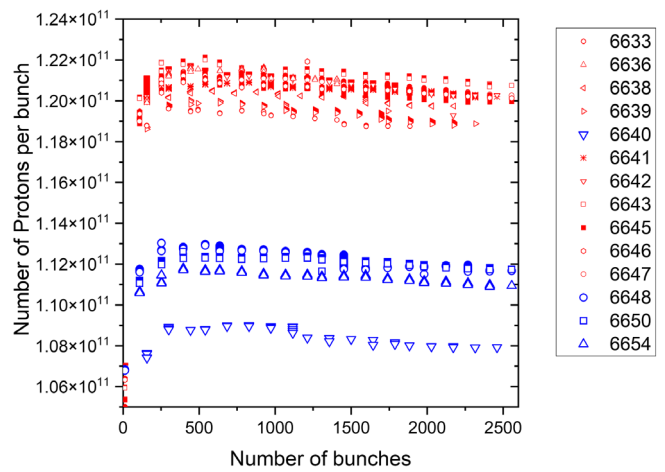


FIG. 5. Evolution of the number of protons per bunch in station 4 (beam 1) as a function of the number of bunches during injection at 450 GeV for several fills (recorded between May 3 and May 7, 2018). Red symbols correspond to fills for which a pressure increase during injection is observed, blue symbols are related to fills for which no pressure increase occurred.

exceeds a threshold:  $1.14 \times 10^{11}$  p + /bunch for fills 6633 to 6654, recorded between May 3 and May 7, 2018,  $1.119 \times 10^{11}$  p + /bunch for fills 7080 to 7274, recorded between August 23 and October 9, 2018. The first value is obtained for fills just after the scrubbing run; the second one is observed toward the end of the physics run period. A surface conditioning effect that would exist just at the start of the physics run period could explain these different thresholds. In the second investigated period, the EC buildup (and therefore the associated pressure increase)

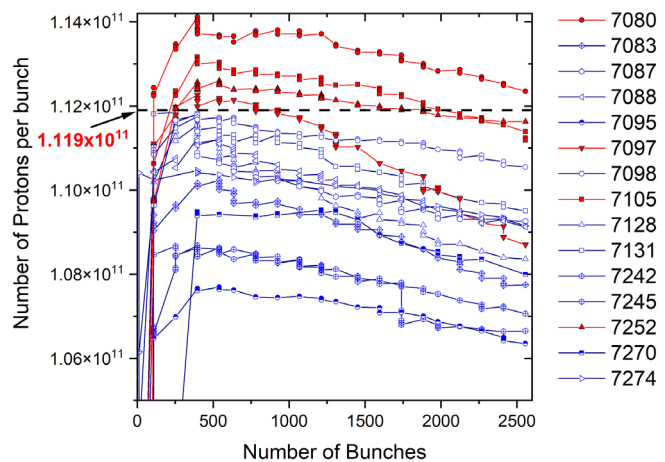


FIG. 6. Evolution of the number of protons per bunch in station 4 (beam 1) as a function of the number of bunches during injection at 450 GeV for several fills (recorded between August 23 and October 9, 2018). Red lines and symbols correspond to fills for which a pressure increase during injection is observed, and blue lines and symbols are related to fills for which no pressure increase occurred.

is very sensitive to the nppb: a tiny variation above the threshold value (some  $10^8$  p<sup>+</sup>/bunch more) leads to the EC formation and the increase in pressure. It is worth noting that once the nppb exceeds the threshold, the rise of pressure starts and continues even if the nppb further returns below this threshold. To conclude, limiting the nppb during the beam injection step below this threshold would prevent a pressure rise.

### C. Decrease of pressure during p-p collisions (at 6500 GeV with synchrotron radiation)

The step corresponding to p-p collisions was also investigated (therefore in the presence of synchrotron radiation). The effect of synchrotron radiation (SR) is superimposed to that produced by EC since the beam energy during this period is 6500 GeV, i.e., above the SR production threshold. In this step, the pressure which was maximum at the end of the energy ramp gradually decreases, as does the electron current measured on the various electrodes. Figure 3 shows that the electron current measured on the three electrodes of station 4 decreases in the same way, independent of the measuring electrode. Such a current decrease indicates that the electron density, and therefore the EC phenomenon, is decreasing progressively during the p-p collision period. The stimulated desorption by electrons, therefore, decreases, also leading to the drop in pressure.

However, it can be seen that the recorded electrical currents (and therefore the electronic density) decrease faster than the pressure. This phenomenon is observed for all investigated fills, for example, during fills 7105 and 7128 (Fig. 3). If the evolution of the pressure is compared to the electron density, both are superimposed at the beginning, and the pressure is proportional to the intensity of the electron current. This evolution continues until the electron density decreases faster than the pressure.

The nppb also decreases gradually due to the collisions between the two beams which take place at the different interaction points (LHCb, ATLAS...). Figure 7 shows that the pressure decreases rapidly with the nppb for several fills in station 4. However, a change in the slope of the pressure as a function of the nppb can be distinguished from an almost identical threshold for all selected fills. This threshold is estimated at  $1.2 \times 10^{11} - 1.0 \times 10^{11}$  p<sup>+</sup>/bunch. It could separate two different regimes (indicated in Fig. 7) in which the pressure decrease is controlled by two different processes.

In view of these observations, the following scenario can be imagined: (i) after the energy ramp, the photoelectron production due to the SR is high for a high beam intensity. Conditions are therefore favorable to produce an intense EC and a high electron density in station 4, leading to a significant electron stimulated desorption and a high pressure. The electron density gradually decreases with the nppb (and with time), and the pressure decreases

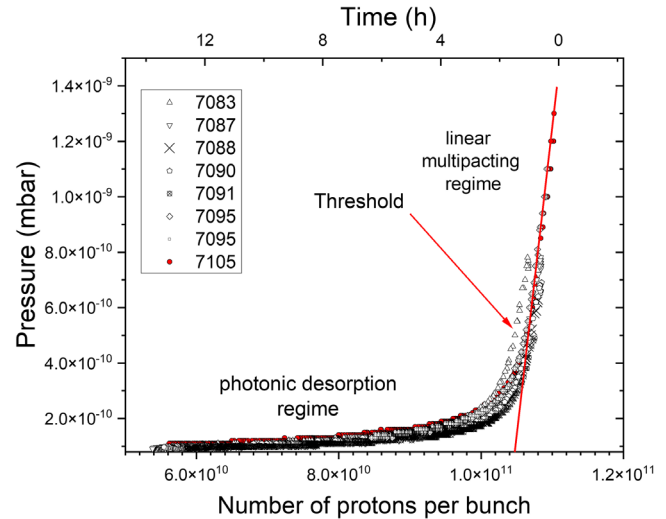


FIG. 7. Variation of pressure with the number of protons per bunch during the p-p collision step with 6.5 TeV/beam for several standard physics fills.

linearly with the electron density (linear multipacting regime). Additionally, the fluxes of photons produced by SR are also intense, and the photon desorption is superimposed on the electron desorption. But, as long as the electron density is high (above  $10^{11}$  p<sup>+</sup>/bunch), the electron desorption dominates and drives the pressure. Moreover, electrons are more efficient than photons to desorb molecules [12]. Then, when the electron density becomes weak, the photon stimulated desorption becomes preponderant, and the pressure is then controlled by the latter (photon desorption regime). Therefore, the results show that the pressure evolution during p-p collisions follows two regimes: a first one in which the stimulated electron desorption predominates, for high nppb; a second one in which photon desorption takes place when the nppb falls below a given threshold (the EC disappears).

### D. Detection of a positive current

#### 1. Experimental data

Figures 2 and 8 show examples of positive currents recorded by electrode K6517A when it is negatively polarized during several fills ( $V_{\text{bias}} = 1000$  V for fill 7319, and  $V_{\text{bias}} = -800$  V and  $-1000$  V for fills 7221 and 7328 respectively). The positive current measured is low, which is indicated by the fact that the signal from this electrode is very noisy. However, as it was previously indicated, the positive current of the K6517A electrode follows the same evolution as the pressure and the electron current: a first peak during the injection followed by a second bump during the energy ramp, then a slow decrease during the proton-proton collisions step.

When the electrode K6517A is negatively polarized, the collected current is the sum of several contributions (ions, electrons, or SE), depending on the applied bias. To

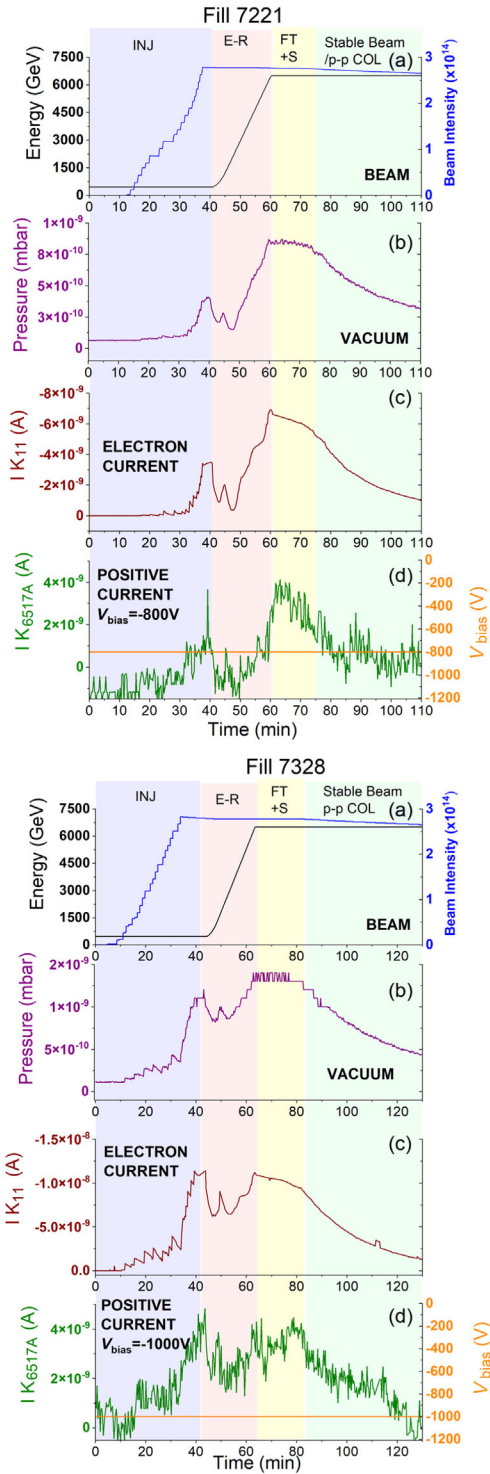


FIG. 8. Measurements performed in station 4 of the VPS during fills 7221 and 7328. Beam 1 parameters (a), pressure (b), electron current (c), positive current (d); (INJ = injection, E-R = Energy, Ramp, FT + S = Flat, Top, and Squeeze).

determine whether ions are actually detected, it is necessary to discriminate these contributions. For this purpose, we calculated the intensity that would be measured by a negatively polarized electrode by determining the current

of SE as a function of (i) the energy distribution of incident electrons impacting the electrode; (ii) the SEY of the electrode. The comparison of the calculations with the experimental measurements is useful to conclude the presence of ions in significant quantities.

## 2. Calculation of the secondary electron contribution to the positive current

The total current  $I_{\text{Tot}}$  collected by the electrode when the bias is negative and is given by

$$I_{\text{Tot}}(E, V_{\text{bias}}, \delta) = I_{e^-}(V_{\text{bias}}, E)I_{\text{SE}}(V_{\text{bias}}, E, \delta). \quad (3)$$

$I_{e^-}$  corresponds to electron current impinging the wall ( $I_{e^-} < 0$ ). Only electrons with sufficient energy  $E$  to overcome  $V_{\text{bias}}$  are collected (since  $V_{\text{bias}} < 0$ ).

$I_{\text{SE}}$  represents the current due to the secondary electrons (SEs) emitted from the surface when electrons impinge the electrode. Usually,  $I_{\text{SE}} = \delta \times I_{e^-}$ , where  $\delta$  is the secondary electron yield (SEY) of copper (the electrode material).

$I_{\text{ion}}$  is the positive ion current collected by the electrode, which is assumed to be independent of the applied negative bias.

Note that the electron currents are negative and the ion currents are positive so that what enters the electrode is added (primary electron current and ions intensity) and what leaves the electrode is subtracted (SE intensity).

If SEY is larger than 1, the term  $(I_{e^-} - I_{\text{SE}})$  is always positive for a negative electrode polarization. Hence, it is not straightforward to separate ion and SE contributions from the total current ( $I_{\text{Tot}}$ ). Moreover, the ion current should be very low compared to the electron signal since the equilibrium ion densities were estimated to be many orders of magnitude smaller than the electron densities [13].

The contribution of primary and secondary electrons to  $I_{\text{Tot}}$  (when  $V_{\text{bias}} < 0$ ) was computed using the MATHEMATICA code. The outcome of the calculations is compared to the experimental signals in order to determine whether a sufficiently large ion flux impinging the beam pipe walls gives a detectable ion current.

*Calculation of the intensity measured by a negative biased electrode.*—The intensity measured by the electrode, if all incident (or primary) electrons are collected, is given by

$$I_{e^-} = K \int_0^{\infty} n(E)dE, \quad (4)$$

where  $n(E)$  is the normalized energy distribution of the electrons impinging the wall and  $K$  is a constant converting an electron density to a current. An energy spectrum of electrons impacting the copper liner in station 4 was previously recorded by Buratin [10,11] with the EKD electrode, during the stable beam period of a standard fill

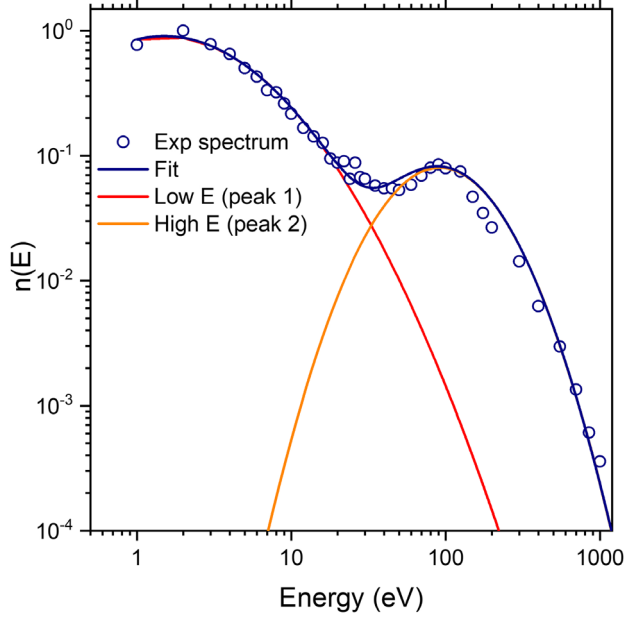


FIG. 9. Normalized energy spectrum of electrons  $n(E)$  (blue open circle) recorded by the EKD electrode in station 4 during a fill at 6500 GeV (data with courtesy of Elena Buratin). Lines are fit to experimental data with Eq. (6): total spectrum (blue line), low energy part (red line), and high energy part (green line).

at 6.5 TeV (Fig. 9). This spectrum exhibits two components: (i) the low energy peak (around 3–5 eV), which constitutes the main population, corresponds to the electrons reaching the wall without having been accelerated by a proton bunch (secondary electrons and photoelectrons at low energy); (ii) the high energy bump (at  $\approx 150$ –200 eV) is related to the electrons accelerated by the beam, which contribute to the multipacting. These features are closed to those calculated by the `PyECLOUD` code for a SEYmax of 1.5 (25-ns bunch spacing, 7-TeV proton beam, see e.g., [4,14]).

To perform the computation, the energy spectrum is described as the sum of two “lognormal” distributions:

$$n(E) = n_1(E) + n_2(E) \quad (5)$$

$$n_i(E) = \frac{K_i}{(\sqrt{2\pi}) \times w_i \times E} \times e\left(-\frac{(\text{Log}[\frac{E}{E_c}])^2}{2w_i^2}\right). \quad (6)$$

A lognormal distribution was chosen since it corresponds to the initial energy distribution of the secondary electrons produced under the impact of incident electrons [4]. It is thus a simple way to analytically express the electron energy distribution in the beam pipe. Equation (5) was used to fit the experimental energy spectrum. The values of the parameters  $E_{c_i}$ ,  $w_i$  and  $K_i$  (for both distributions) are reported in Table I. Figure 9 shows the energy spectrum fitted with Eq. (5).

When the electrode is polarized with a negative bias, the electrons with an energy  $E$  lower than the bias (in absolute

TABLE I. Values of the parameters obtained from the fit to the experimental electron energy spectrum.

Parameters	Peak 1	Peak 2
$E_c$ (eV)	6	150
$K$	7.9	16.5
$w$ ( $\text{eV}^{-1}$ )	1.17	0.7

value) are repelled, only those with higher energy reach the electrode. Figure 10 shows an example in which  $V_{\text{bias}} = 40$  V: the electrons whose energy corresponds to the hatched area are not collected. The incident electrons measured by the electrode have energy equal or higher than  $|V_{\text{bias}}|$ .

When a negative bias is applied to the electrode, the intensity of the incident electron current is then written as

$$I_{e^-}(E > |V_{\text{bias}}|) = K \int_{|V_{\text{bias}}|}^{\infty} n(E) dE. \quad (7)$$

The intensity of the primary electrons calculated with Eq. (7) decreases progressively with the bias that is applied to the electrode. This behavior is due to the fact that the population of electrons declines as their energy is further increased and the majority of electrons come from the low energy part of the electron energy distribution.

A negatively biased electrode acts as a retarding field so that the energy  $E_i$  of electrons impacting the electrode surface is  $E_i = E - |V_{\text{bias}}|$ . Therefore the SE current emitted from the surface by these impinging electrons is given by

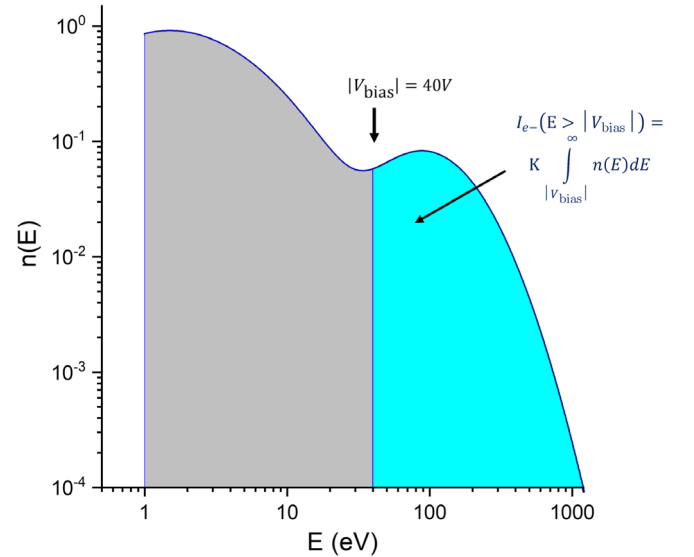


FIG. 10. Normalized energy spectrum of electrons  $n(E)$  as a function of energy. The blue part corresponds to the contribution of electrons to the intensity recorded by an electrode polarized at  $V_{\text{bias}}$ .

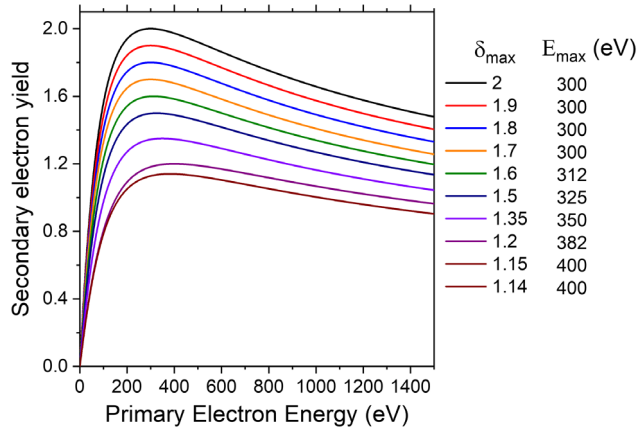


FIG. 11. SEY curves calculated for copper using Eq. (10) with different values of  $\delta_{\max}$  and  $E_{\max}$ .

$$I_{\text{SE}}(E, V_{\text{bias}}, \delta) = K \int_{|V_{\text{bias}}|}^{\infty} \delta(E - |V_{\text{bias}}|) \times n(E) dE, \quad (8)$$

where  $\delta$  is the secondary electron yield (SEY) of the copper electrode. The electron current measured by an electrode with a negative bias is thus finally given by

$$\begin{aligned} I_{e-}(E, V_{\text{bias}}) - I_{\text{SE}}(E, V_{\text{bias}}, \delta) \\ = K \int_{|V_{\text{bias}}|}^{\infty} n(E) [1 - \delta(E - |V_{\text{bias}}|)] dE. \end{aligned} \quad (9)$$

*Influence of the Secondary Emission Yield.*—An expression of the SEY given by Scholtz in [15] can be used to numerically express the variation of the secondary electron yield as a function of the primary electron energy:

$$\delta(E) = \delta_{\max} \frac{s \times \left(\frac{E}{E_{\max}}\right)}{s - 1 + \left(\frac{E}{E_{\max}}\right)^s}. \quad (10)$$

For the LHC beam chambers, a value of  $s = 1.35$  can be used [4].  $\delta_{\max}$  corresponds to the maximum value of the SEY and  $E_{\max}$  is the corresponding energy. SEY plots for different values of  $E_{\max}$  and  $\delta_{\max}$  are presented in Fig. 11. The progressive decrease of  $\delta_{\max}$  for the different SEY plots is related to the surface conditioning (often called scrubbing). This effect is observed when the surface is exposed to prolonged electron irradiation and occurred for the copper wall in the LHC [16,17].

The calculated total electron current [Eq. (9)] can be normalized to the total incident electron current (4) as

$$I_{\text{norm}} = \frac{\int_{|V_{\text{bias}}|}^{\infty} [n(E)(1 - \delta(E - |V_{\text{bias}}|))] dE}{\int_0^{\infty} n(E) dE}. \quad (11)$$

This normalization allows one to directly compare the computed electrical current to the experimental one (with the electrode polarized with a negative bias).

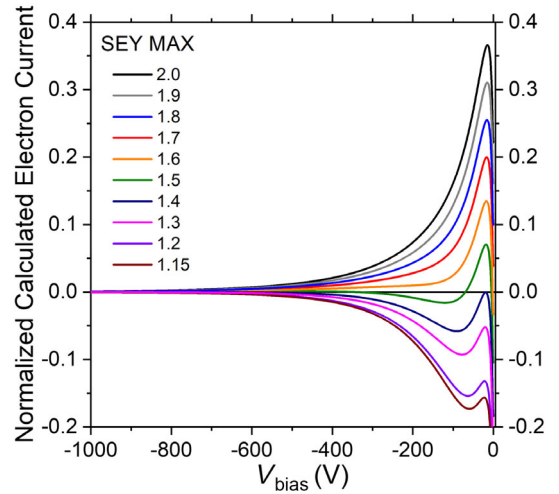


FIG. 12. Variation of the electron current vs  $V_{\text{bias}}$  calculated for several SEY using Eqs. (10) and (11) with normalization.

Figure 12 shows the intensity of the calculated electron current which should be measured by the electrode (when a negative bias is applied) as a function of  $\delta_{\max}$ . The energy spectrum used for this calculation is the one presented in Fig. 10. The intensity becomes positive for electrode SEYs larger than 1.4, indicating that the contribution of SE (i.e., positive current contribution) is predominant for the highest values of the SEY. As shown, a first rapid increase of the calculated intensity is observed for bias ranging from 0 to about  $-25$  V, a maximum value is reached in the range  $[-25$  V,  $-15$  V], then a progressively decreases of the intensity occurs to vanish above  $-500$  V. This result indicates that no electron signal should be detected for a bias lower than  $-500$  V.

*Influence of the electron energy distribution.*—The advantage to describe analytically the electron energy distribution is that the fitting parameters of the spectrum can be modified to investigate the influence of the electron distribution shapes on the computed intensity. Figure 13 shows different energy spectra with different parameters (displacements on peak 2 toward higher energy or greater contribution of accelerated electrons than those of the experimental spectrum).

Figure 14 presents an example of calculated intensities with new energy spectra as a function of a negative bias. These calculations were performed with the maximum value (1.7) of the SEY. As seen in these plots, on one hand, when the contribution of the accelerated (primary) electrons increases (i.e., increase in the intensity of peak 2), but their average energy remains the same, a rise in the intensity of the electron current (dotted blue lines in Fig. 14) is observed. On the other hand, if the energy of the accelerated electrons is progressively increased (the maximum of peak 2 shifts toward higher energy), their contribution increases strongly for low absolute values of

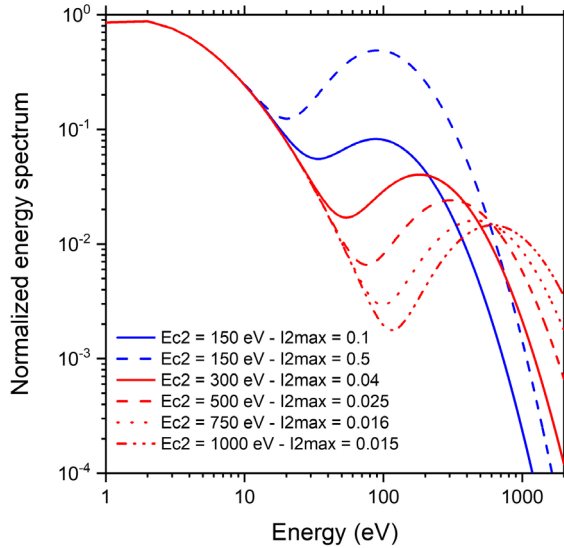


FIG. 13. Energy spectra calculated with different parameters for peak 2 (the position of the peak is displaced at higher energy or its intensity is modified).

the bias, leading to a large broadening of the electrode intensity (red lines in Fig. 14).

### 3. Comparison between experimental and calculated values

The computed current (corresponding to the contribution of both primary and secondary electrons) and the experimental one (that may include an additional ion contribution) must be normalized to the primary electron current in order to allow a comparison. Therefore, the positive signal recorded with the electrode K6517A, when it is negatively

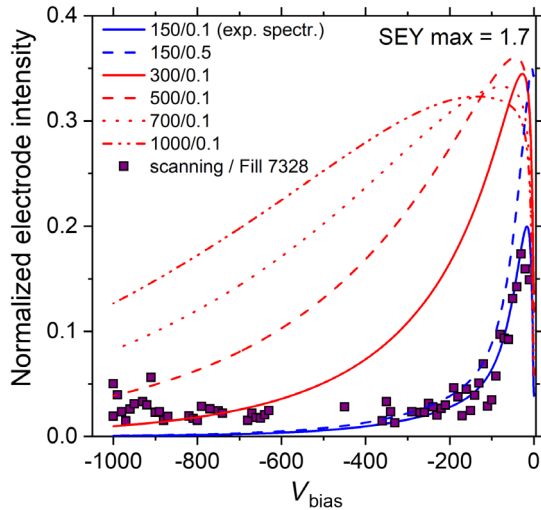


FIG. 14. Comparison between calculated intensities from different energy spectra and a maximum SEY of 1.7 (lines), and experimental data (purple squares) recorded on the electrode K6517A for a negative bias scanning performed during fill 7328.

polarized, is divided by the primary electron current measured with the K11 electrode (positively polarized at +9 V to record the total primary electron current), corrected using Eq. (1).

The current was recorded by the electrode K6517A during scanning of  $V_{\text{bias}}$  from 0 to  $-1000$  V after the energy ramp up (6500 GeV) of fill 7328. After normalization, this signal is plotted in Fig. 14 as a function of bias, and it is compared to the plots calculated with different electron energy spectra. A better agreement is obtained with the experimental spectrum presented previously in Fig. 9, indicating that the high energy component of the electron energy distribution is located around 100–150 eV and not at higher energy. Despite the discrepancy appearing for the low values of the bias (from  $-600$  to  $-1000$  V—see Fig. 14), the experimental spectrum is the only one that correctly reproduces the shape and the experimental variations observed in the bias range between 0 and  $-200$  V. Thus, this result confirms the use of the experimental electron energy distribution in station 4 to perform the calculations presented thereafter.

The range in which the bias varies between 0 and  $-200$  V can be examined in more detail. The current was recorded for several scanning of  $V_{\text{bias}}$  from 0 to  $-127$  V after the energy ramp-up (6500 GeV) for fill 6640 (two scans) and fill 7328. The comparison between experimental outcomes and calculations with several SEYs is presented in Fig. 15 (computation performed with the experimental electron energy spectrum). The normalized electrode intensity rises initially with decreasing bias voltage ( $V_{\text{bias}}$ ), up to a maximum value reached for  $V_{\text{bias}} \approx 20$  V, and then declines as  $V_{\text{bias}}$  is further decreased. For the scans recorded during fill 6640, the experimental data are in good agreement with the curves calculated with

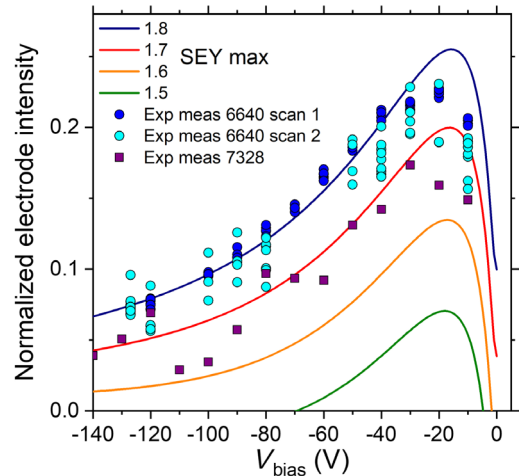


FIG. 15. Variation of the normalized electrode intensity vs  $V_{\text{bias}}$ . Experimental data (blue circles and purple squares) were recorded during fills 6640 and 7328, and values were calculated using the experimental electron energy spectrum and several SEY (color lines).

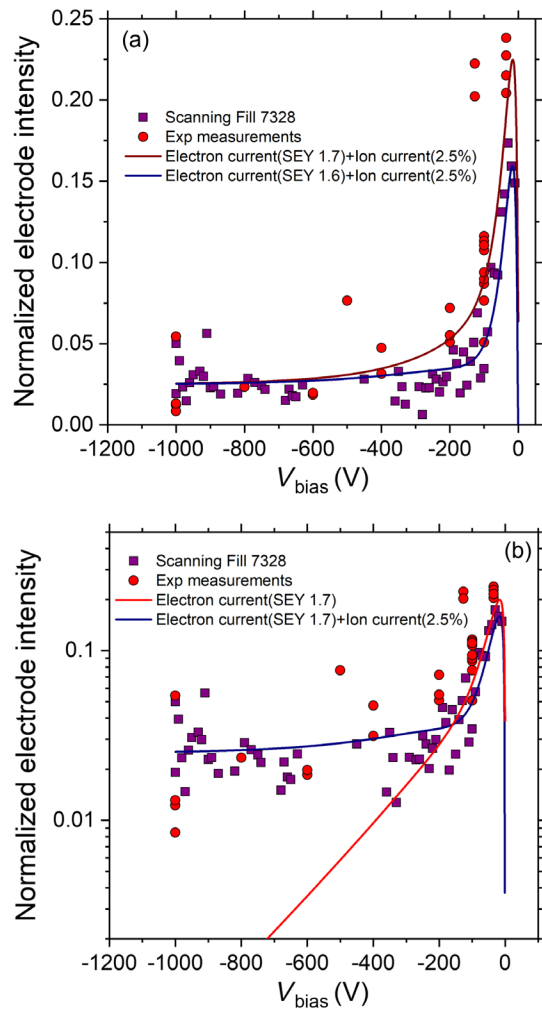


FIG. 16. Normalized electrode intensity vs  $V_{\text{bias}}$ . Experimental data recorded during several fills (red circles) or during fill 7328 (purple squares) are compared to calculated intensities by adding 2.5% of positive ions and taking a SEY of 1.6 (blue line) or without ions and taking a SEY of 1.7 (red line): linear (a) or logarithmic (b) y axis.

a maximum SEY between 1.7 and 1.8, whereas for fill 7328, the SEY seems to be lower (1.7). In this bias range  $[0, -140 \text{ V}]$ , the positive intensity is dominated by the secondary electrons emitted from the electrode surface, while being bombarded by primary electrons.

The positive current recorded by the electrode during different fills does not change very much over time for a given negative bias. For example, the bias scanning carried out during fill 6640 is only marginally different from that recorded during fill 7328, whereas the first one was carried out in May 2018 and the last one in October 2018. This result indicates that the conditioning of the electrode surface in station 4 is not significant. Thus, the secondary electron emission of the copper electrodes remains constant during the studied period.

As shown in Fig. 16, for an extended scanning from 0 to  $-1000 \text{ V}$  performed during fill 7328, a discrepancy

between calculated and experimental signals occurs above  $V_{\text{bias}} = 500 \text{ V}$ , whereas the calculated signal for the electrons vanishes at the lowest  $V_{\text{bias}}$  values, experimental measurements reach a low but constant value, which could correspond to a positive ion current.

To confirm the presence of ions, current measurements were performed during several fills, just after the energy ramp-up, with  $1000 \text{ V} \leq V_{\text{bias}} \leq 0 \text{ V}$  (Fig. 16). The results clearly show that below  $-400 \text{ V}$ , a constant positive value is reached. As the signal from primary electrons and SE should be zero at the lowest  $V_{\text{bias}}$ , the remaining signal can only be related to positive ions. The measurements are normalized to the incident electron current (obtained with the electrode K6517A). Thus, the measured ion current corresponds to 2.5% of the incident electron current. If this constant ion current is added to the calculated electron current, it is seen that the maximum SEY of the copper electrode should be between 1.6 and 1.7 (Fig. 16). It is worth noting that positive ions can also produce an electron emission, which may affect the determination of the ion intensity.

#### IV. DISCUSSION AROUND DYNAMIC PRESSURE ANALYSIS

##### A. Pressure and electrical currents

Pressure, electron, and ion currents follow the same global evolution during a standard fill for physics. However, differences in behavior can occur in a specific step. For instance, during the injection step of the proton beam into the ring, an increase in pressure and electrical currents is measured in station 4 for some fills, but no significant change is observed for other fills, whereas the filling pattern scheme seems to be the same. By analyzing our measurements recorded during the proton injection step (for a beam of 450 GeV and the standard filling pattern), it can be shown that an EC buildup appears when the number of protons per bunch becomes greater than a threshold (of the order of  $1.12 \times 10^{11} \text{ p}^+/\text{bunch}$ ). This result means that the electron density must rapidly increase to produce a significant rise in pressure, induced by electron stimulated desorption (and possibly by ion induced desorption).

If the EC buildup does not occur, the electron density remains low and the ionization of the residual gas by the proton beam is not sufficient to provide the electron flux necessary to produce desorption and a significant pressure rise. Likewise, the flux of ions generated by the ionization of the residual gas is also too low to be detected. A significant ion current is measured only when the electron density itself is high. The predominant source of ion production is therefore the ionization of the residual gas by the electrons of the EC.

The ionization of the residual gas by the proton beam is not large enough to produce a substantial quantity of electrons and therefore a rise in the pressure was observed

during the proton beam injection step. The pressure increases and the ion production in the beamline is thus driven by the electron density of the EC. During the energy ramp-up, the photoelectrons produced by the SR add to the electrons originating from residual gas ionization to finally produce multipacting. The maximum photon flux calculated in the VPS is around  $6 \times 10^{14}$  ph/m/s. Conditions for the formation of an EC buildup during a standard fill for physics at top energy are met to produce an EC since a rise in pressure (and electron currents) is always observed during this step. When the beam is stable and the sequence of p-p collisions begins, the electron desorption drives the pressure and the photon-desorption does not seem to have a visible effect as long as the EC is observed. The drop in the electron density during the beginning of this step induces a decrease in pressure. Then this one is only related to the photon-desorption at the end of the p-p collision sequence since the intensity of the EC becomes too low to affect the pressure. It is worth noting that, as the EC is always formed at the end of the energy ramp, the ionization of the residual gas by electrons provides also ion fluxes of sufficient intensity to be detected.

In conclusion, the evolution of the electron density related to the EC buildup drives both the increase in the pressure (production of neutral particles by electron stimulated desorption) and the number of ions (the residual gas is mainly ionized by electrons).

### B. Secondary emission yield

From the measurements performed in the VPS, the secondary electron yield of the copper electrode in station 4 was estimated to be 1.6. This value appears to be higher than expected. The SEY parameter was inferred for LHC arc beam screens by comparing the heat load measured at 450 GeV with the operational 25 ns beam configuration against EC buildup simulations performed with the `PyECLOUD` code [18]. Results predict lower SEY values after beam surface conditioning in the different LHC arcs: between 1.18 and 1.32. However, no magnetic field is present in the VPS, in contrast to the LHC arcs. Thus, the expected SEY threshold for multipacting may be larger. This point was confirmed by `PyECLOUD` calculations applied to the VPS, showing that in this case, the threshold SEY to trigger the EC is about 1.4 [19].

It is worth noting that the SEY determined in station 4 corresponds to one of the copper electrodes used to measure electrical currents. One could notice that it should not be representative of the SEY of the liner copper wall, due to (i) electrode transparency; (ii) the positive bias applied to the electrode to repel electrons since in this case, the electron dose received by the electrode would be lower than the dose received by the wall of the vacuum chamber. First, if the electron dose is normalized to the area impinged by electrons, the dose per surface unit is independent of the

transparency. Second, the time during which the electrode has been negatively biased represents less than 1% of the operating time of the accelerator, and therefore this effect on the surface conditioning is negligible. Therefore, the SEY estimated in station 4 should be globally the same for electrodes and the vacuum chamber wall. Moreover, no large decrease in the pressure and the electron current in station 4 was observed during machine operation from May to October 2018 indicating that no large decrease in the SEY of the liner copper wall is thus expected during this period as observed for the copper electrodes.

### V. CONCLUSION

The investigation of the dynamic vacuum in the LHC via measurements performed in the VPS provides a global understanding of the complex desorption phenomena involved in the beamlines during machine operation leading to unexpected pressure evolutions.

The results reported in this paper deal with the pressure variation and electrical signals (arising from both ions and electron clouds) measured in station 4 of the VPS (beam 1, unbaked copper) during standard fills for physics in the LHC. It was found that the electron cloud buildup starts during the proton beam injection step (standard filling scheme) when the number of protons per bunch threshold of  $\approx 1.12 \times 10^{11}$  p<sup>+</sup>/bunch is exceeded. During the p-p collision step, the pressure evolution is driven by both the photo- and the electron-stimulated desorption. For the first time, positive ions were detected at higher rates than expected from beam-gas ionization (2.5% of the incident electron current). The comparison of calculations and experimental results allow us to determine a SEY of 1.6 for the copper surface in station 4. No specific conditioning effects were highlighted during the last period of RUN II (from May to October 2018), in agreement with the rather high value of SEY. These results also explain that an electron cloud activity is always measured at the end of RUN II in station 4 of the VPS. Finally, the pressure increase and the ion production were shown to be mainly driven by electrons from the electron cloud.

All the measurements performed in the VPS and the different outcomes show the importance to take into account several unexpected phenomena in order to understand the pressure evolution in the LHC. These results are useful to find out solutions allowing to mitigate beam instabilities in the LHC and also for the conception and the building of future colliders.

### ACKNOWLEDGMENTS

The authors are grateful to E. Buratin and F. Letellier for their assistance during the experiments. This work was supported by the Memorandum of Understanding for the Futur Circular Collider Study (Grants No. FCC-GOV-CC-0004 and No. EDMS 1390795).

- [1] O. Brüning, P. Collier, P. Lebrun, S. Myers, R. Ostojic, J. Poole, and P. Proudlock, Large Hadron Collider (LHC) design report, CERN Yellow Report No. CERN-2004-003-V-1, CERN, Geneva, 2004.
- [2] L. Evans and P. Bryant, LHC machine, *J. Instrum.* **3**, S08001 (2008).
- [3] F. Zimmermann, Electron cloud effects in the LHC, in *Proceedings of the Mini Workshop on Electron Cloud Simulations for Proton and Positron Beams*, CERN, Geneva, Switzerland (CERN, Geneva, Switzerland, 2002), pp. 47–55.
- [4] G. Iadarola, Electron cloud studies for CERN particle accelerators and simulation code development, Report No. CERN-THESIS 047, 2014.
- [5] G. Rumolo and F. Zimmermann, Electron cloud simulations: Beam instabilities and wakefields, *Phys. Rev. ST Accel. Beams* **5**, 121002 (2002).
- [6] E. Buratin, V. Baglin, and B. Henrist, Preliminary results obtained with the LHC vacuum pilot sector, in *Proceedings of the Joint INFN-CERN-ARIES Workshop on Electron-Cloud Effects (ELOUD'18)*, 2018, *La Biodola, Isola d'Elba, Italy* (2020), Vol. 7, 10.23732/CYRCP-2020-007.
- [7] P. A. Anderson, The work function of copper, *Phys. Rev.* **76**, 388 (1949).
- [8] V. Baglin, G. Bregliozzi, G. Lanza, and J. M. Jimenez, Synchrotron radiation in the LHC vacuum system, Report No. CERN-ATS-2011-245, 2011, <https://cds.cern.ch/record/1407539>.
- [9] B. Henrist, V. Baglin, G. Bregliozzi, and P. Chiggiato, The LHC vacuum pilot sector project, in *Proceedings of the 5th International Particle IPAC2014, Dresden, Germany, 2014* (CERN, Geneva, Switzerland, 2014) (Report No. CERN-ACC-2014-0264, 2014), 10.18429/JACoW-IPAC2014-WEPME042.
- [10] E. Buratin, V. Baglin, B. Henrist, P. Chiggiato, and A. Fasioli, Electron flux and pressure dynamic in the LHC vacuum pilot sector as a function of beam parameters and beam pipe properties, *Phys. Rev. ST Accel. Beams* **23**, 114802 (2020).
- [11] E. Buratin, Electron Cloud and Synchrotron Radiation characterization of technical surfaces with the Large Hadron Collider Vacuum Pilot Sector, Thesis, Ecole Polytechnique de Lausanne, 2020.
- [12] O. Malyshev, Vacuum in Particle Accelerators: Modelling, Design and Operation of Beam Vacuum Systems (Wiley-VCH Verlag GmbH & Co., KGaA, New York, 2020).
- [13] G. Rumolo and F. F. Zimmermann, Interplay of ionization and sputtering with the electron Cloud, Report No. CERN-SL-2001-014-AP, 2001, <https://cds.cern.ch/record/501409>.
- [14] G. Skripka, P. Dijkstal, G. Iadarola, L. Mether, G. Rumolo, and E. Wulff, Comparison of electron cloud build-up simulations against heat load measurements for the LHC Arcs with different beam configurations, in *Proceedings of the 10th International Particle Accelerator Conference, IPAC-2019* (JACoW, Geneva, Switzerland, 2019), 10.18429/JACoW-IPAC2019-WEPTS051.
- [15] J. J. Scholtz, D. Dijkkamp, and R. W. A. Schmitz, Secondary electron emission properties, *Philips J. Res.* **50**, 375 (1996).
- [16] N. Hilleret, G. Vorlauffer, V. Baglin, I. Collins, and B. Henrist, A summary of main experimental results concerning the secondary electron emission of copper, Report No. CERN-LHC-Project-Report-472, 2001.
- [17] R. Cimino, M. Comisso, D. R. Grosso, T. Demma, V. Baglin, R. Flammini, and R. Larciprete, Nature of the Decrease of the Secondary-Electron Yield by Electron Bombardment and its Energy Dependence, *Phys. Rev. Lett.* **109**, 064801 (2012).
- [18] G. Iadarola, G. Skripka, M. Albert, D. Amorim *et al.*, Beam-induced heat loads on the LHC arc beam screens with different beam and machine configurations: Experiments and comparison against simulations, Report No. CERN-ACC-NOTE-2019-0057, 2019.
- [19] G. Iadarola (private communication).